Graphical Abstract

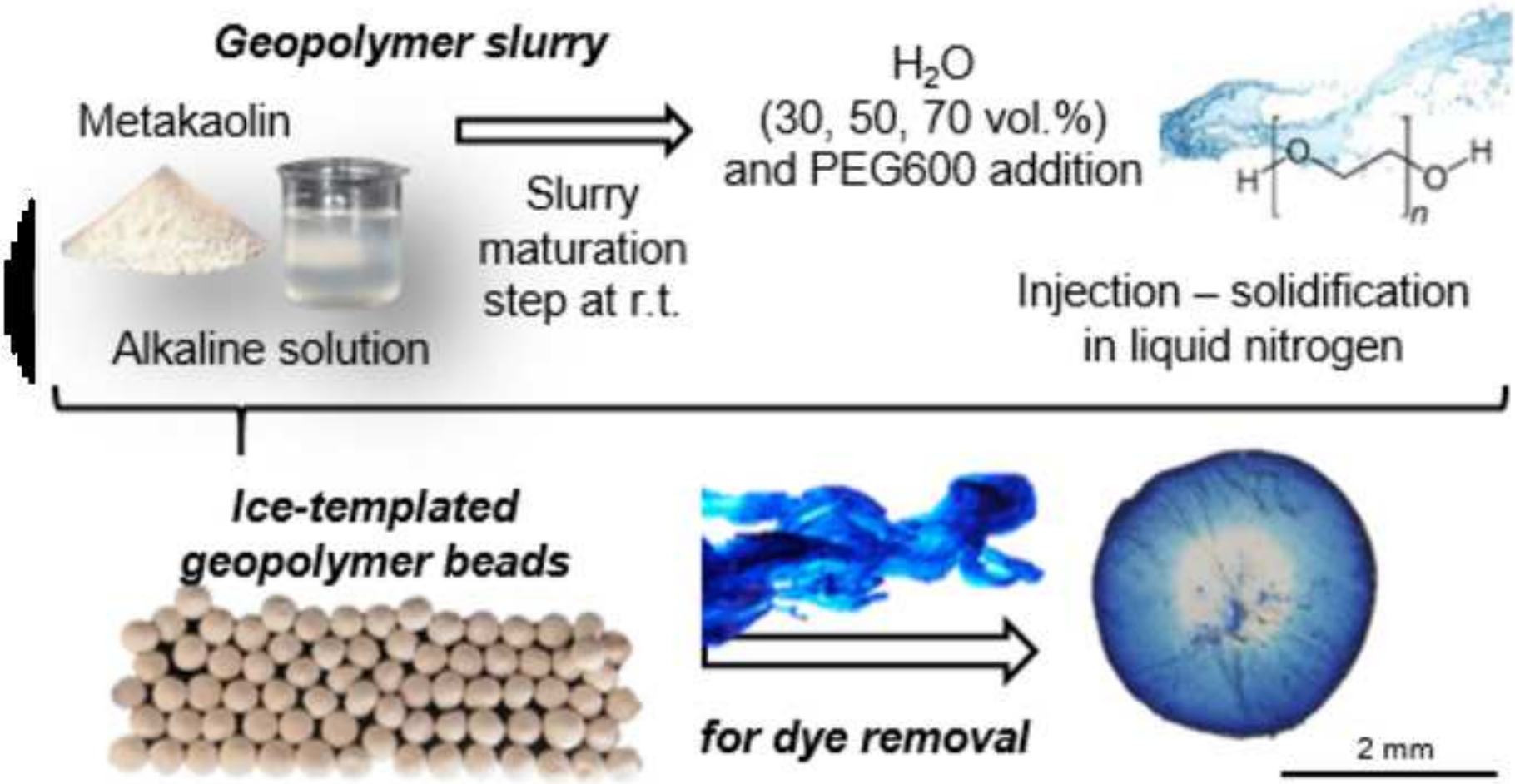

Doi: https://doi.org/10.1016/j.jcis.2020.03.104

Ice-templated geopolymer beads for dye removal

Elettra Papa, Matteo Mor, Annalisa Natali Murri, Elena Landi, Valentina Medri*

National Research Council of Italy, Institute of Science and Technology for Ceramics (CNR-ISTEC), Via Granarolo 64, 48018 Faenza, RA, Italy

*Corresponding author e-mail: elettra.papa@istec.cnr.it

Abstract

Geopolymer beads, conceived as alternative low cost adsorbents for wastewater treatment, were shaped by a dripping technique in liquid nitrogen, through an ice-templating process. PEG600 was added as a binder to ease the process, standardizing the beads dimension. The beads were investigated in terms of morphology, microstructure and mechanical strength, following compressive tests by ISO 18591. Functional tests, to verify the adsorption capacity, were conducted using methylene blue (MB) with different concentrations and for different contact time. The removal efficiency was mainly related to the morphology and porosity of the beads, which in turn was directly related to the water content added to the geopolymer slurry. In general, all beads reached an average removal efficiency of 98% after 24 h. However, the best performing beads were able to uptake MB very quickly, attaining a removal efficiency of 76% after only 30 minutes.

Keywords: geopolymer, beads, injection-solidification, ice-templating, adsorption, wastewater treatment

1. Introduction

The reclamation of wastewater needs treatment technologies which are efficient, well established, simple to operate and affordable, as adsorption. Indeed, adsorption is an effective technology to counteract the drawbacks of those industrial and agricultural activities that have led to a remarkable discharge of pollutants into the environment, in particular of dyes and heavy metals in water streams [1]. Adsorption is largely used due to its simplicity, ease of operation and high adaptability, therefore absorbents with different geometries and chemical compositions have been studied for dyes removal [2]. Because activated carbons are the most efficient adsorbents, thanks to a unique and large adsorption capacity, but have a high production cost [3], the research is focusing on cheaper and "greener" alternatives. Among them, geopolymers have attracted attention thanks to their many interesting properties, in particular ionic exchange and to the eco-friendly nature of their production process.

Geopolymers are inorganic polymers, a class of synthetic alkali-aluminosilicate materials easily obtained through a water-based chemical reaction between an aluminosilicate powder and a highly alkali aqueous solution [4]. Sustainable development goals have encouraged advances in geopolymer materials because they can be synthetized at relatively low temperature, from room temperature up to 80 °C, utilizing also industrial and agricultural wastes [5].

Nanoprecipitates and mesopores compose the final 3D network that is negatively charged because of the presence of Al in tetrahedral coordination [6-7]. Commonly, cations as sodium and potassium balance the network, endowing the material with ionic exchange properties in analogy with zeolites, their crystalline counterpart [4,8]. Thus, the porous structure and the ion

exchange capacity suggest their use as dyes or heavy metals adsorbents, as already reported in literature [9-11]. Furthermore, geopolymers can be shaped through several techniques, with the possibility of tuning their porosity on a large dimensional range [12-13]. Studies have often focused on the use of powders as adsorbents, which present a series of drawbacks, as the difficult recovery, the impossibility to be used in packed beds, the need to be supported in industrial application and the need of a separation step after the wastewater treatment [14]. All these issues are detrimental to the wastewater treatment cost and increase the process complexity. For these reasons, the design of an adsorbent in a compact spherical shape, as a bead, can be beneficial in these terms.

This paper reports the production of porous geopolymer beads obtained through an injection-solidification method in liquid nitrogen, conceived as low cost, green, easy-to-produce adsorbents for the treatment of wastewater. The beads porosity is thus formed by a sacrificial templating method in which a frozen liquid phase (ice) acts as a template for the pores, resulting advantageous from the environmental point of view [15-16].

Geopolymer beads for adsorption purposes have been already produced by other groups [14, 17-19], but injection-solidification method in liquid nitrogen was reported only by the present authors [20-21]. This paper explores how some process parameters can affect the final properties of the beads obtained through this technique.

A potassium-based geopolymer mixture has been added with different water amounts to vary the beads porosity by the ice-templating process. A binder (PEG600) was also used to facilitate the formation of the beads.

The beads were characterized in terms of morphology, microstructure, mechanical resistance, porosity and specific surface area. Functional tests, to verify their adsorption capacity, were performed using methylene blue as cationic model dye.

2. Materials and methods

2.1 Materials and beads preparation

A potassium di-silicate solution, with molar ratio H_2O:K_2O=13.5 and SiO_2:K_2O=2.0, was prepared as the alkali activating solution, by dissolving KOH pellets (> 85%, Sigma Aldrich) in deionized water and adding fumed silica (99.8%, Sigma Aldrich) under magnetic stirring.

Metakaolin Argical™ M1200S (SSA= 25 m^2 g^{-1}, d50= 1.5 μm) was purchased from Imerys. The chemical composition of the metakaolin was the following: Al_2O_3=39.0%, SiO_2=55.0%, Fe_2O_3=1.8%, TiO_2=1.5%, K_2O/Na_2O=1.0%, and crystalline phases such as quartz and small amounts of muscovite were present as inert impurities [22].

The theoretical SiO_2:Al_2O_3 molar ratio of the geopolymer slurry was fixed equal to 4.0 [7,23], while K_2O:Al_2O_3 molar ratio was equal to 0.8; metakaolin powder was mixed at 900 rpm for 5 minutes with a stoichiometric amount of potassium di-silicate solution using a planetary centrifugal mixer (THINKY MIXER ARE-500) at room temperature. Subsequently, the slurry underwent a maturation step of 4h at room temperature, already reported in [24-25], in order to foster the geopolymerization process without reaching a complete consolidation.

After maturation, distilled water in different amount (30, 50, 70 vol.% over the theoretical volume of the geopolymer solid matrix plus the added water, considering a geopolymer density of 2.2 g cm^{-3}) was added to the slurry and mixed with the planetary mixer for 3 minutes at 900

rpm plus 1 minute at 1200 rpm following a defoaming step. Some samples were also added with PEG600 (Merck), a soluble polymer frequently used in freeze casting to improve the structural integrity of the materials acting as binding agent. PEG600 was previously blended with water prior to be mixed with the aged geopolymer slurry, in the amount of 3 wt.% over the geopolymer dry weight. The samples were coded G-x, where x is 30, 50, 70, depending on the vol.% of extra water. When PEG600 was added, the beads were coded G-x-P. The codes of the geopolymer beads are reported in Table 1.

The different slurries were then directly dripped in a liquid N_2 bath using a peristaltic pump (speed 3 rpm) with a nozzle of 0.8 mm diameter. The droplets were instantly frozen into beads, collected and put in a freeze dryer set at −40 °C (Edwards Mod.MFD01, Crawley, UK), where the formed ice crystals were sublimated (-40 °C /+25 °C, P= $8 \cdot 10^{-2}$ torr). The beads were then cured for 24h at 60 °C and a final washing treatment (24h in a deionized water bath + drying in a heater at 60 °C) was applied to remove eventually non-reacted phases.

2.2 Characterization techniques

Morphological analysis was performed on high resolution images, using the open access program ImageJ and measuring the average major and minor beads diameter, the area and the roundness (expressed as 4*Area/(π* major axis^2)) of 200 beads for each different batch.

The microstructural features of the beads were examined by an Environmental Scanning Electron Microscope (E-SEM FEI Quanta 200). The samples were previously made conductive applying a thin gold layer using a turbo-pumped sputter coater (Quorum Q150T ES).

Mechanical tests were performed at room temperature simultaneously on several beads using a die-plunger test according to the international standard ISO 18591. The test was carried out using

a universal testing machine (Zwick Z050, loading cell class 05, GmbH, Ulm, Germany) and a cross-head speed of 1 mm min^{-1}. The beads were subjected to uniaxial compressive loading in a confining steel die, under specified ISO conditions. The mechanical test was repeated 3 times for each bead type. The applied standard allowed to calculate the average compressive strength (P_c) and the density of the compressed beads (ρ_c), the latter calculated applying Eq.1:

$$\rho c = \frac{}{V} = \frac{}{\{A \cdot [h+(lf-l)]\}} \qquad (1)$$

where:

ρ_c = density of the die-pressed compact;

m = mass of the die-pressed compact;

V = volume of the die-pressed compact;

A = base area of the die-pressed compact;

h = height of the die-pressed compact;

l_f = overall displacement of the piston;

l = displacement of the piston over time.

Pore size distribution of the beads in the range 0.0058–100 μm was analyzed by mercury intrusion porosimetry, MIP (Thermo Finnigan Pascal 140 and Thermo Finnigan Pascal 240). The experimental error was mainly due to the accuracy of the method (4%).

The measurement of the specific surface area has been carried out on the beads in a Thermo Scientific™ Surfer instrument. The specific surface area was calculated by the Brunauer–Emmett–Teller (BET) method, by means of nitrogen adsorption at 77 K. The experimental error of this measurement is mainly due to the specific surface analyzer (1%).

Adsorption tests were conducted using the cationic dye methylene blue (MB) as a model molecule, in order to calculate the removal efficiency and the adsorption capacity.

A 2000 ppm stock solution was prepared and hereafter diluted to the desired concentrations (10, 50 ppm) used for the adsorption tests. For the tests, 100 ml of dye solution were used with a 1g of geopolymer beads kept under mechanical agitation during the test.

The removal efficiency was calculated using Eq.2:

$$\text{Removal Efficiency (E) (\%)} = \frac{C0-Ct}{C0} \text{x}100 \qquad (2)$$

Where C0 and Ct are the initial and time t concentrations (M), respectively.

The adsorption capacity was calculated using Eq.3, quantifying the MB uptake by the geopolymer beads in mg MB/g geopolymer:

$$\text{Adsorption capacity (q)} = \frac{(C0-Ct)\ \text{x}\ V}{} \qquad (3)$$

where q is the amount of dye adsorbed by the geopolymer beads, V is the volume (L), and m is the geopolymer mass of the beads (g).

The concentrations of the MB solutions before and during the tests were measured using an UV-spectrophotometer (LAMBDA 750 UV/Vis/NIR Spectrophotometer, PerkinElmer) by measuring the absorbance at λ=664 nm. The measurements have been taken at regular time intervals.

The morphological and macrostructural features of the beads after the MB adsorption tests were investigated by digital microscopy (3D Digital Microscope RH2000, Hirox, Japan).

3. Results and discussion

3.1 Morphology and Microstructure of the beads

As already observed in previous works [21, 24-25], the main issue with injection-solidification method in liquid nitrogen and with the ice-templating applied to geopolymers is the stop of the geopolymerization reaction when the slurry gets in contact with the liquid N_2 or the cold

substrate, because water (the reaction medium) freezes and turns into ice. To overcome this issue, a "maturation step" must be adopted before, to initiate the geopolymerization without reaching a complete consolidation of the mixture [24-25]. Indeed, during the maturation step, the mixture starts to consolidate and increases its viscosity, making it hard to extrude the slurry through the needle. Water, in different amount 30-50-70 vol.%, must then be added to the aged mixture to ease the dripping process and increase the final porosity of the beads, deriving by the ice-templating process.

In general, the adopted process parameters allowed to obtain uniform and porous beads with spherical shape and a roundness value between 0.92 and 0.94 (Table 1), approaching the perfect roundness value of 1.

Spherical beads are obtained when droplets initially levitate on liquid N_2, following the inverse Leidenfrost effect [26]. Droplets levitate because heat passes from the (relatively warm) drop to the liquid bath beneath it and, in doing so, causes the liquid to evaporate, leading to the formation of a supporting vapor layer [26]. The temperature of the droplet decreases until it first freezes itself (releasing latent heat of fusion in the process), before further cooling and ultimately reaching the Leidenfrost temperature of the liquid N_2. At this point, film boiling ceases, the vapor layer disappears, and the droplet sinks into the bath [26].

The beads were investigated by image analysis and the average major and minor diameter (Ø), area and roundness values calculated were reported in Table 1, while the major Ø distributions for the different types of beads are reported in Figure 1.

The addition of 30 vol.% of water (G-30) allowed to obtain compact and more regular spherical beads, with a major Ø distribution centered at lower values, between 1.8 and 3.0 mm (Figure 1a). More irregular beads, with a wider major Ø distribution, centered between 2.8 and

4.4 mm (Figure 1a) and a less spherical shape (lower roundness value, Table 1) were obtained increasing the amount of water up to 70 vol.%.

Table 1. Samples code and water added for the ice-templating process of the produced beads. Average major and minor diameter, area and roundness values calculated by image analysis on 200 beads of each type.

Sample Code	H_2O (vol.%)	Major Ø (mm)	Minor Ø (mm)	Area (mm^2)	Roundness
G-30	30	2.86 ± 0.13	2.70 ± 0.13	6.08 ± 0.54	0.94 ± 0.04
G-30-P	30	2.54 ± 0.15	2.40 ± 0.13	4.80 ± 0.51	0.94 ± 0.03
G-50	50	3.22 ± 0.21	2.98 ± 0.20	7.56 ± 1.01	0.93 ± 0.05
G-50-P	50	3.08 ± 0.22	2.89 ± 0.18	7.02 ± 0.92	0.94 ± 0.03
G-70	70	3.18 ± 0.21	2.92 ± 0.24	7.32 ± 1.00	0.92 ± 0.05
G-70-P	70	3.26 ± 0.22	3.00 ± 0.24	7.70 ± 1.00	0.92 ± 0.06

The bead shape and dimension depend on the starting mean droplet size that in turns depends on the needle diameter and on several parameters as the surface tension, density and viscosity of the slurry ejected from the needle [27], that were not in deep investigated in this article. However, an easy correlation between the density of the slurry and the final size of the beads could be found. A higher water content in the mixture lowers the density of the slurry, therefore, since the pressure of the peristaltic pump and the needle diameter are fixed, it will be dripped more easily, with formation of bigger droplets. Moreover, a higher water content generates more ice nucleation, resulting in an expansion of the beads. Furthermore, the shape of the final beads is affected by the deformation that droplets can encounter when in contact with the liquid N_2. In this case, a less dense slurry offers less resistance and the beads tend to be deformed. These

aspects justify the bigger dimensions and the irregular major Ø distributions (Figure 1a) of G-50 and G-70 beads.

The addition of the binder PEG600 resulted in an increase of the regularity of the major Ø distributions of the beads, all included between 1.8 and 3.7 mm (Figure 1b). Beads were more compact and spherical, with a lower diameter than beads without PEG (Figure 1a). PEG affects the viscosity of the slurry, consequently the droplets formation. The polymer acts as a part of the solid loading, resulting in the increase of the viscosity, as well as a larger force the freezing front could experience during the solidification of the liquid vehicle [28]. Therefore, the droplets are deformed with more difficulty when dripped in liquid N_2 bath, showing a more regular shape.

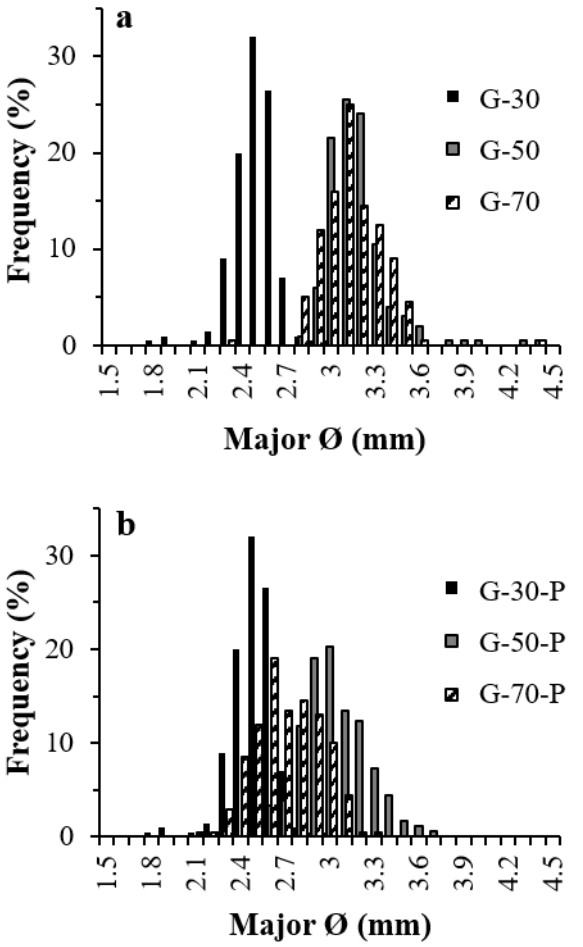

Figure 1. Major diameter distribution for beads G13-30, G13-50, G13-70 (a) and of the same formulations with the addition of PEG600 (b).

SEM images of the whole beads and of their cross section, with and without PEG, are reported in Figure 2 and Figure 4, respectively. The beads external and internal microstructures, at higher magnification, are showed in Figure 3 and Figure 5. Externally all beads appear compact, smooth and dense, while the cross sections show a radial porosity derived from the ice-templating process. The water added after the maturation step acted as a pore-forming agent creating oriented porosity inside the beads [29]. The porous structure developed in a radial way aligning

along the temperature gradient inside the beads, because the freezing occurred from the external part, directly in contact with liquid N_2, towards the warmer center of the beads.

Droplets are subjected to the inverse Leidenfrost effect as well as to an abrupt phase change from liquid to solid when cooled down [30]. The surface of a droplet comes in contact with liquid N_2 first, and it cools down more quickly than the inner region. Therefore, the rapid freezing can generate surface vitrification, that is a phase transition of a liquid to a glass (amorphous ice) with a very low degree of crystallization [30], generating a smooth and dense surface. The degree of crystallization of droplets is a function of the composition, concentration of solutes and droplet size that affect the heat diffusion in the droplet, developing more or less ice nucleation [30].

Observing the internal microstructures of the beads G-30, G-50 and G-70 (Figure 3d,e,f), it is evident that the increase of water vol.% generates a more porous microstructure, promoting the radiality and the formation of dendritic patterns. This is more evident for G-70 (Figure 3f) which shows a highly porous microstructure also on the external part (Figure 3c), in contrast with the denser surface of G-30 (Figure 3a). The external surface of G-50 (Figure 3b) is in part similar to that of G-30 (Figure 3a) and in part to that of the more porous G-70 (Figure 3c), because of the different thermal resistance generated in the droplets.

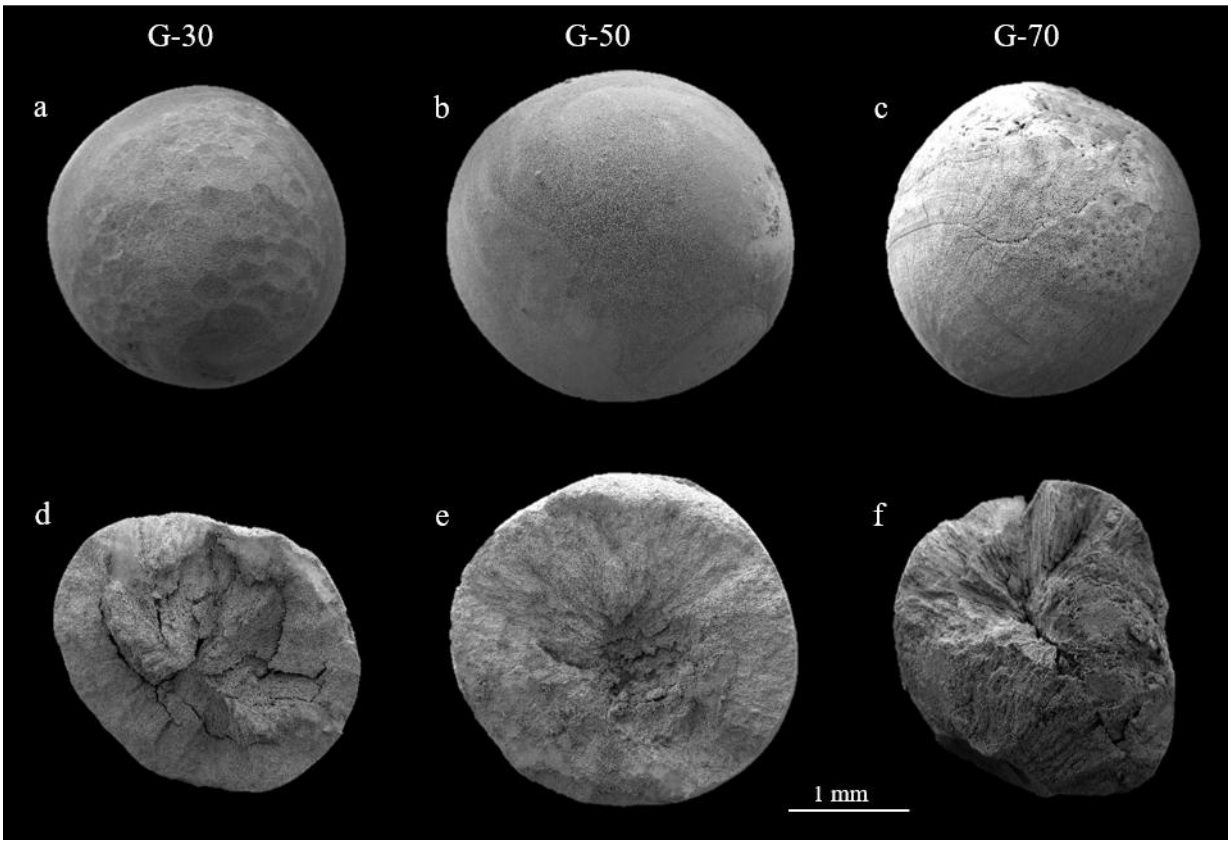

Figure 2. SEM micrographs of integer beads (a,b,c) and cross sections (d,e,f) of G-30 (a, d), G-50 (b,e) and G-70 (c,f).

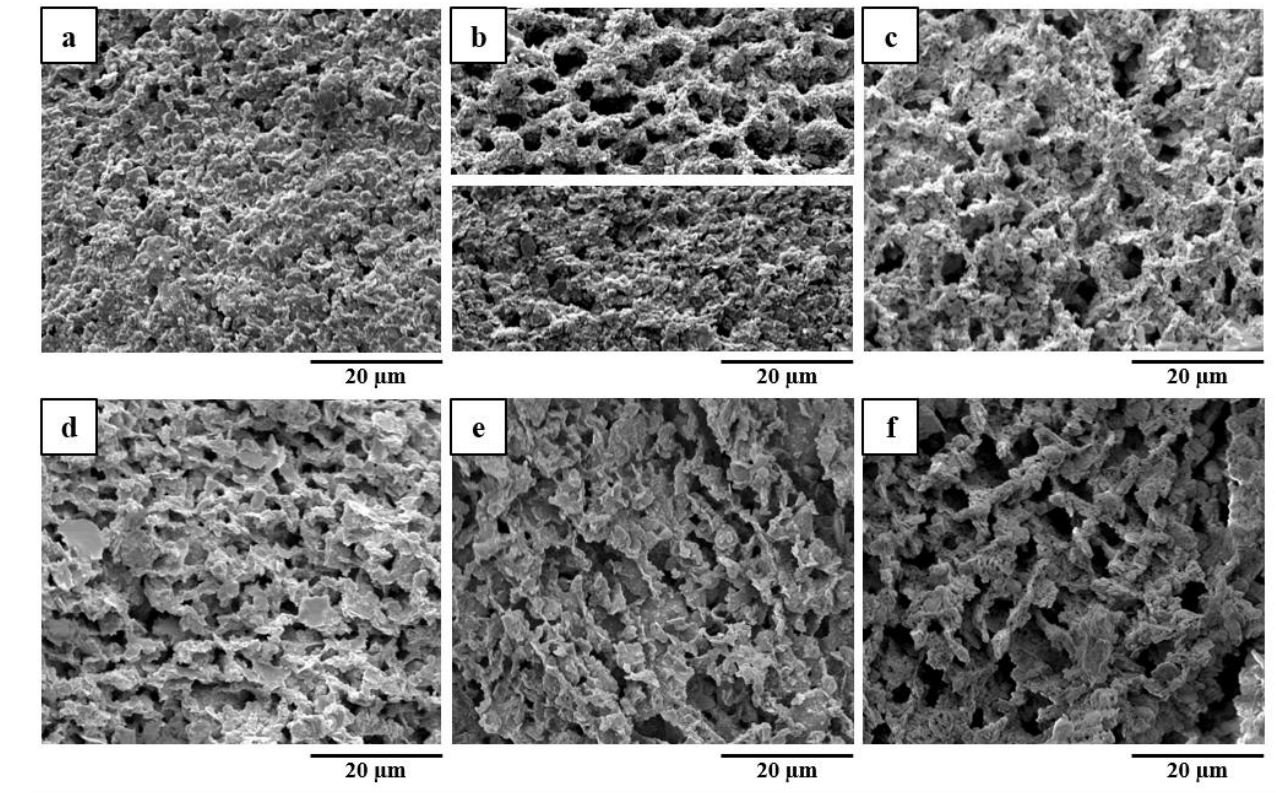

Figure 3. SEM micrographs of the external (a,b,c) and internal (d,e,f) surfaces of G-30 (a,d), G-50 (b,e) and G-70 (c,f).

The addition of PEG600, as mentioned before, affected the viscosity, the solidification process and, as a consequence, the porosity of the beads [31-32].

Comparing the whole beads and the cross sections reported in Figure 2 and Figure 4, it is evident that the presence of PEG helped in the spherification process, allowing the formation of regular beads. Generally, the introduction of additives to the ice-templating system influences the pore structure by changing the ice solidification behaviour (modifying the freezing temperature and ice expansion), limiting the diffusion of water molecules and particle expulsion.

This is particularly noticeable for sample G-30-P (Figure 5a,d) that showed the presence of rounded macropores of about 10 µm on the external and internal surface of the bead, due to PEG removal during the washing treatment. Indeed, the low water content (30 vol.%) promoted the

development of a high density material, with consequent poor homogeneous PEG dissolution. This effect was less pronounced for the other samples because the increased water amounts diluted the binder, avoiding its concentration in spherical droplets.

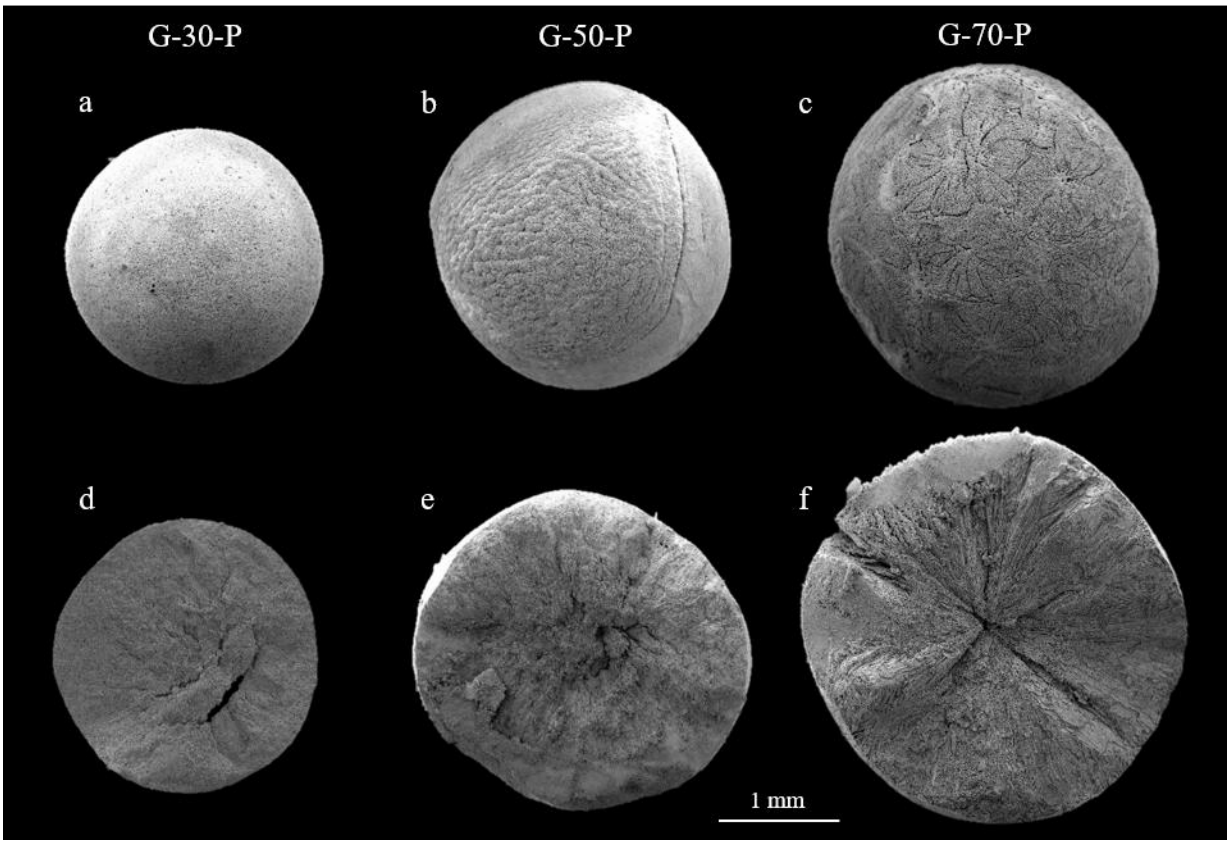

Figure 4. SEM micrographs of integer beads (a,b,c) and cross sections (d,e,f) of G-30-P (a,d), G-50-P (b,e) and G-70-P (c,f).

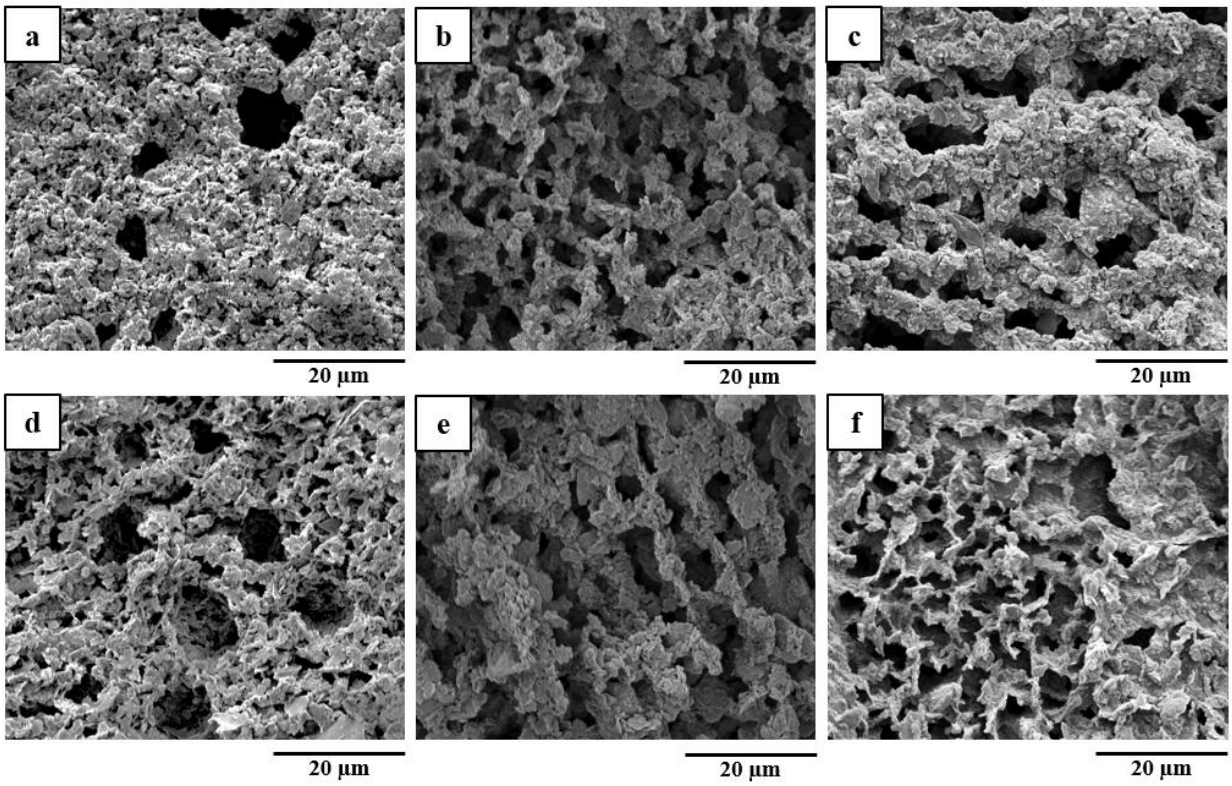

Figure 5. SEM micrographs of the external (a,b,c) and internal (d,e,f) surfaces of G-30-P (a,d), G-50-P (b,e) and G-70-P (c,f).

3.2 Porosity and specific surface area

Values obtained through MIP and SSA values are reported in Table 2, while MIP pore size distributions of the different beads are shown in Figure 6. MIP takes into account mainly the small pores developed in the geopolymer matrix and the smallest pores obtained through the ice-templating process. As predictable from the microstructural evaluations, an increase of the water amount led to an increase of the total intruded pore volume, porosity % and an enlargement of the pore size. In fact, water acts as a pore former agent in the geopolymer matrix, and affects the macroporosity produced in the material by the ice-templating method. It is well evident as the total intruded volume (and porosity %) increased with increasing the water content, passing from 574 $mm^3 g^{-1}$ (57%) for G-30, to 824 $mm^3 g^{-1}$ (66%) for G-50, to 1011 $mm^3 g^{-1}$ (69%) for G-70.

Table 2. Porosity values by mercury intrusion porosimetry (MIP) and specific surface area (SSA) by nitrogen adsorption.

Sample	Total vol. ($mm^3 \cdot g^{-1}$)	Porosity (vol.%)	Average Ø (µm)	Modal Ø (µm)	SSA ($m^2 \cdot g^{-1}$)
G-30	574	57	0.09	1.20	107
G-50	824	66	0.20	2.22	63
G-70	1011	69	0.19	2.61	59
G-30-P	545	53	0.08	1.20	12
G-50-P	744	61	0.30	2.16	30
G-70-P	1252	70	0.32	3.60	21

Regarding the pore size distributions (Figure 6), all the beads showed a prevalently monomodal distribution with the most frequent pore size (modal pore Ø, Table 2) located at different dimensional ranges because of the increase of the water amount. Indeed, the modal pore Ø for G-30 is 1.20 µm and increased to 2.22 µm for G-50, up to 2.61 µm for G-70.

Conversely, the specific surface area decreased with the increasing of the water amount, resulting 107 m^2 g^{-1} for G-30, 63 m^2 g^{-1} for G-50 and 59 m^2 g^{-1} for G-70. Indeed, high water contents increase the porosity and promote the formation of bigger pores, decreasing the specific surface area [7].

Regarding the beads with PEG, the values did not differ much from those obtained for the beads without PEG (Table 2). On the other hand, the SSA substantially decreased (Table 2), especially for G-30-P being 12 m^2 g^{-1} compared to 107 m^2 g^{-1} of G-30. The addition of PEG shifted the pore size distribution toward higher values, increasing the contribution of pores bigger than 1 µm, particularly for G-30-P (Figure 6d), probably causing the decrease of surface area values.

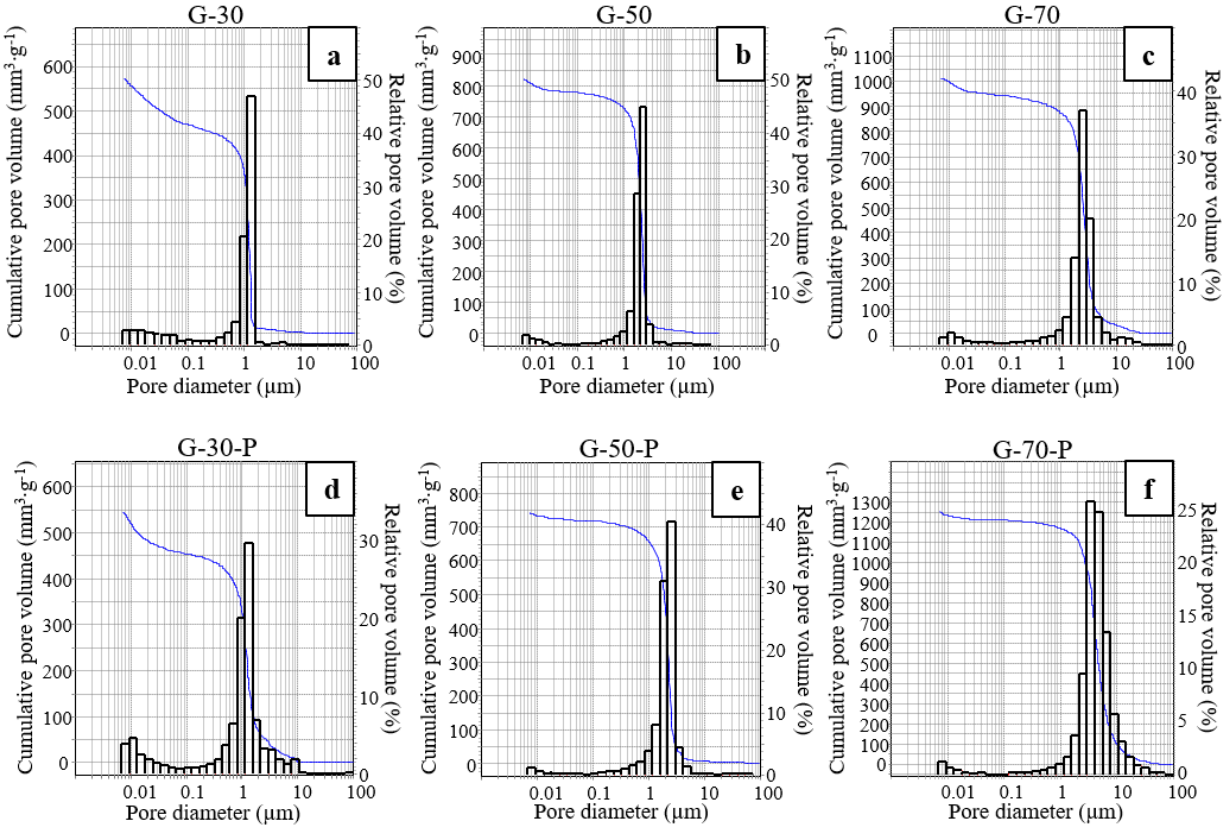

Figure 6. Pore size distribution by Hg intrusion porosimetry (MIP) of G-30 (a), G-50 (b), G-70 (c), G-30-P (d), G-50-P (e) and G-70-P (f).

3.3 Mechanical characterization

Mechanical tests were performed through the compaction of the beads following ISO 18591 standard and obtaining a load-displacement curve that could be converted into pressure-density curve, whose slope change defined the compressive strength of the beads.

In general, when granules (beads in this case) are compacted by uniaxial compression in a die they rearrange during compaction, but when a pressure higher than the critical pressure P_c is applied, deformation and fracture also occur. The final density of the compact depends on the compressive strength (namely the critical pressure P_c) of the beads.

Table 3 reports the critical pressure (P_c) and critical density (ρ_c) calculated for the different beads. The values obtained for G-30, G-50 and G-70 are comparable in the error limit and the relatively low values (between 2.6 and 3.4 MPa) are due to the great porosity as evidenced by MIP analysis (Table 2).

The mechanical test was performed also on G-50-P, for comparison, pointing out as the addition of the binder PEG600 was responsible for an increase of almost twice the mechanical resistance of G-50 samples. Indeed, P_c passed from 3.3 MPa for G-50 to 5.9 MPa for G-50-P. The increase was due to a higher homogeneity of the G-50-P beads, which probably led to a higher compaction into the die.

Table 3. Compressive strength P_c and critical density ρ_c of the different beads obtained according to ISO / DIS 18591.

Sample Code	P_c (MPa)	ρ_c (g cm^{-3})
G-30	2.6 ± 0.8	0.73 ± 0.14
G-50	3.3 ± 1.0	0.81 ± 0.03
G-70	3.4 ± 0.6	0.64 ± 0.15
G-50-P	5.9 ± 1.0	0.74 ± 0.01

3.4 Methylene blue adsorption – functional test

To assess the adsorption properties of the various beads, removal efficiency (E%) and adsorption capacity (q) have been measured, using methylene blue (MB) as a model dye.

The adsorption of MB is due to the ionic exchange between the K^+ counter-cation of the geopolymer and the cationic dye, which generates an electrostatic interaction.

The first test was conducted on G-30, G-50 and G-70 beads using a 10 ppm solution of MB. The trends of q and E as a function of contact time are shown in Figure 7 a,b while Table 4 reports E values recorded at defined time intervals. The main difference between the beads was found in the adsorption speed in the first hour of test. Comparing the values shown in Table 4, it is evident as G-50 and G-70 showed a higher efficiency, equal to 58 and 73% respectively (after only 30 minutes), compared to 45% measured for G-30. Differently, increasing the time, the trends tended to be similar reaching an average removal efficiency of 95% after 20 hours.

The higher E values are due to the higher porosity developed in these beads (Table 2), because of the ice-templating process, as evidenced by MIP analysis. Indeed, a high porosity allowed MB to permeate more rapidly.

Consequently, G-50 and G-70 beads were tested with a more concentrated 50 ppm MB solution and the values compared with those obtained with the corresponding beads added with PEG (G-50-P and G-70-P).

Table 4. Removal efficiency E (%) at different contact time for beads tested with 10 and 50 ppm MB solutions.

Time (min)	E (%) - 10 ppm MB			E (%) - 50 ppm MB			
	G-30	G-50	G-70	G-50	G-50-P	G-70	G-70-P
30	43	58	73	34	37	31	77
60	67	80	85	52	54	54	92
135	91	88	91	77	78	79	96
1200	98	94	94	-	-	-	-
1440	-	-	-	98	97	98	99

The trends of q and E as a function of contact time are shown in Figure 7 c,d. q values are comparable with the absorption capacities of other geopolymer adsorbents reported in literature using the same concentrations of methylene blue [14, 33-34].

Table 4 reports E values recorded at defined time intervals. The trends were all similar, with the exception of G-70-P that showed a really fast uptake of MB, reaching a removal efficiency of 76% after only 30 minutes, in comparison to an average E of 34% for the other beads. This high efficiency was due to the highest porosity (70%) and modal pore Ø (3.60 μm) as well as the homogenous major Ø distribution (Figure 1b) obtained for G-70-P beads. However, all the beads at the end of the test (after 24h) reached an average E of 98%.

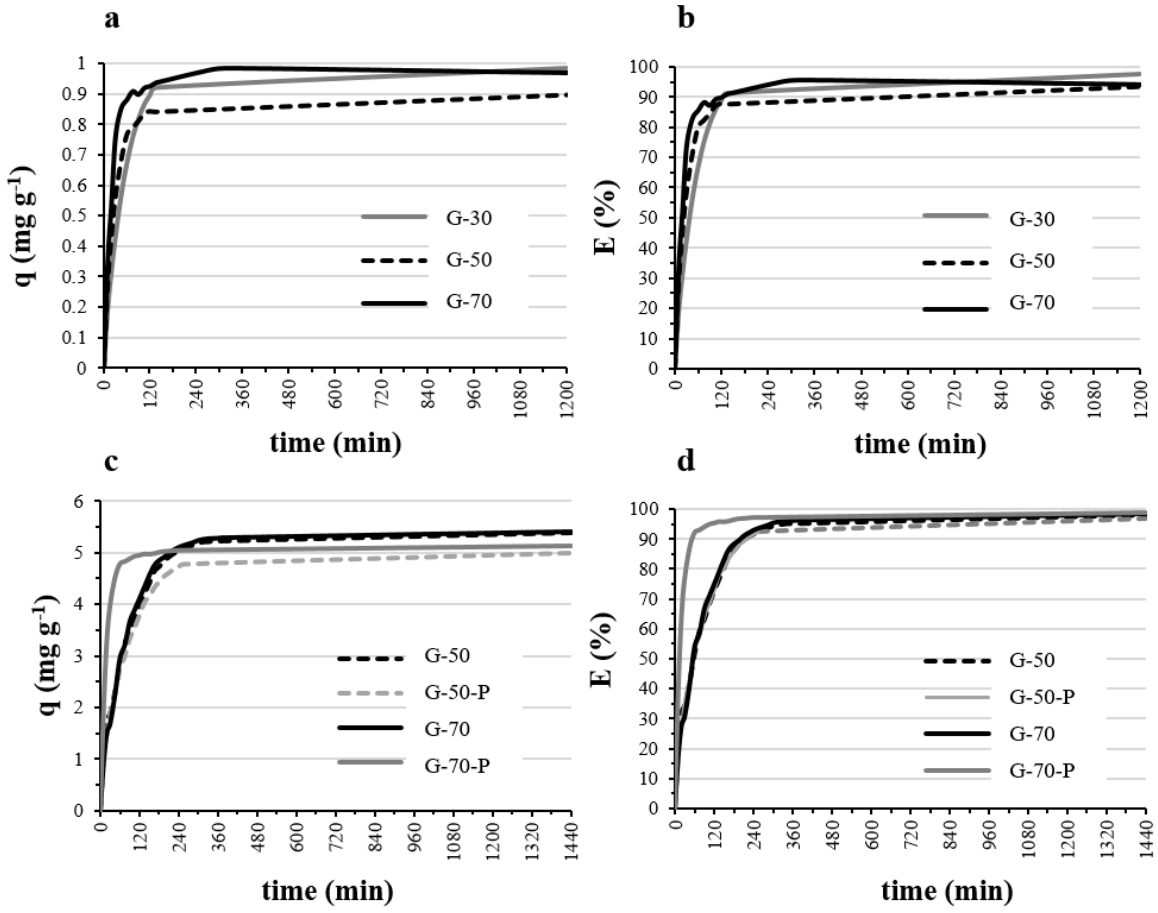

Figure 7. Adsorption capacity q (a, c) and removal efficiency E (b, d) as a function of contact time. Test performed on the beads G-30, G-50, G-70 at 10 ppm MB (a, b) and G-50, G-50-P, G-70, G-70-P at 50 ppm MB (c, d).

A representative comparison of the cross sections of G-50 and G-50-P beads after the MB tests is shown in Figure 8. The image of the three beads after MB adsorption shows how the beads were not completely saturated, with a preferential adsorption on the surface. Therefore, it can be hypothesized that these beads could adsorb a greater quantity of dye per gram of material and the adsorption was limited because of the exhaustion of the dye in the solution. Increasing the MB solution concentration to 50 ppm a significantly higher adsorption was evidenced on the surface,

that resulted dark blue, without reaching its adsorption limit in the internal part also in this case (Figure 8b).

The comparison between G-50 (Figure 8b) and G-50-P (Figure 8c) beads, after the test conducted with MB at 50 ppm, highlighted how the binder influenced the sphericity of the beads but also the development of the porosity, showing how the penetration of the dye had a more homogeneous gradient towards the inner part of the bead (Figure 8c).

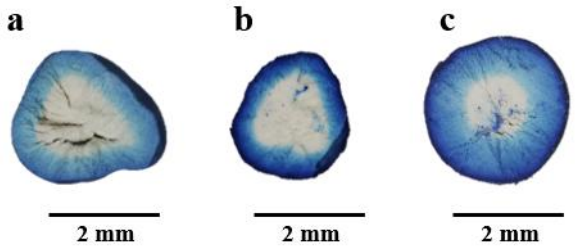

Figure 8. Cross sections of G-50 bead after adsorption test at 10 ppm MB (a) and G-50 (b) and G-50-P (c) beads after test at 50 ppm MB.

3.4.1 Kinetic of MB adsorption onto the beads

The nature of the sorption process depends on physical or chemical characteristics of the adsorbent system and also on the system conditions [35]. In order to investigate the controlling mechanism of adsorption process, the pseudo-first-order and the pseudo-second-order models were used to fit the experimental data reported in Figure 7 [36].

The linear forms of these models are expressed by the following equations:

Pseudo-first-order $q_t = q_e (1- e^{-K_1 t})$ (4)

Pseudo-second-order $q_t = \frac{q_e^2 K_2 t}{1+ q_e K_2 t}$ (5)

where q_t e q_e (mg g^{-1}) are the adsorption capacity of MB at time t and at equilibrium, respectively. K_1 (min^{-1}) and K_2 (g mg^{-1} min^{-1}) are the kinetic rate constant of the pseudo-first-order and pseudo-second-order adsorption, respectively.

The best-fit model was selected based on the linear regression correlation coefficient, R^2 values.

The calculated parameters, for the different models applied, are reported in Table 5 together with the R^2 values.

Table 5. Pseudo-first-order and Pseudo-second-order model parameters, correlation coefficients R^2 and experimental adsorption capacity at equilibrium for adsorption of MB at different concentrations on the beads.

Sample	MB (ppm)	Pseudo-first-order			Pseudo-second-order			Experimental
		K_1 (min^{-1})	q_e (mg g^{-1})	R^2	K_2 (g mg^{-1} min^{-1})	q_e (mg g^{-1})	R^2	q_e (mg g^{-1})
G-30	10	0,0203	1,0014	0,9993	0,0345	1,0093	0,9990	0,9826
G-50	10	0,0207	0,6616	0,9442	0,0752	0,9117	0,9998	0,9009
	50	0,0099	4,4586	0,9859	0,0045	5,6370	0,9974	5,3961
G-70	10	0,0164	2,2403	0,8850	0,0741	1,0265	0,9989	0,9837
	50	0,0108	4,5867	0,9883	0,0046	5,6593	0,9966	5,4033
G-50-P	50	0,0120	4,7022	0,9979	0,0049	5,1706	0,9985	4,9949
G-70-P	50	0,0147	1,6757	0,8299	0,0295	5,1493	0,9999	5,1210

All the beads showed higher R^2 values with the pseudo-second-order model, with the exception of G-30 that presents very similar R^2 values for the pseudo-first and pseudo-second-order.

Considering the pseudo-second-order mechanism, with the assumption that the dye uptake process is due to chemisorption [35], the calculated q_e values are in great agreement with the experimental q_e obtained from the adsorption test as showed in Table 5.

4. Conclusion

This study explores the use of an injection-solidification method in liquid nitrogen to obtain millimeter size geopolymer beads, conceived as alternative and easy-to-produce adsorbents for the treatment of wastewater.

It was possible to take advantage of both the geopolymer mesoporosity and the porosity derived by the ice-templating process by properly combining the maturation step of the geopolymer slurry together with the extra water added for the ice-templating process. The addition of different water vol.% affected the pores morphology, influencing the adsorption properties.

In general, the peculiar ion exchange properties of the geopolymer allowed to uptake MB through a chemisorption, as highlighted by the adsorption kinetic that follows a pseudo-second-order model. While, the addition of high amounts of water (50, 70 vol.%) made it possible to obtain highly porous beads, but with irregular size distributions, able to promote a faster MB adsorption.

The use of a binder as PEG600 was helpful to obtain more spherical beads with a controlled size distribution and a higher mechanical resistance. In fact, the compressive strength almost doubled comparing G-50 (3.3 MPa) with G-50-P (5.9 MPa).

The combination of PEG and 70 vol.% of added water allowed to obtain the best performing beads, which showed a fast uptake of MB with a removal efficiency of 76% after only 30 minutes. However, all the beads reached an average removal efficiency of 98% after 24h test.

The good results of removal efficiency and the non-complete saturation of the beads after the tests put in evidence the potential of the beads, also towards other types of pollutants. Therefore, the best performing beads will be further tested.

Acknowledgement

The authors greatly thank Mr Cesare Melandri for mechanical test.

References

[1] K.C. Lai, L.Y. Lee, B.Y.Z. Hiew, S. Thangalazhy-Gopakumar, S. Gan, Environmental application of three-dimensional graphene materials as adsorbents for dyes and heavy metals: Review on ice-templating method and adsorption mechanisms, J. Environ. Sci. 79 (2019) 174-199.

[2] M.T. Yagub, T.K. Sen, S. Afroze, H.M. Ang, Dye and its removal from aqueous solution by adsorption: A review, Adv. Colloid Interface Sci. 209 (2014) 172-184.

[3] A.E. Burakov, E.V. Galunin, I.V. Burakova, A.E. Kucherova, S. Agarwal, A.G. Tkachev, V.K. Gupta, Adsorption of heavy metals on conventional and nanostructured materials for wastewater treatment purposes: A review, Ecotox. Environ. Safe. 148 (2018) 702-712.

[4] J. Davidovits, Geopolymers chemistry and applications, Geopolymer Institute, Saint-Quentin, France, 2008

[5] N. Asim, M. Alghoul, M. Mohammad, M.H. Amin, M. Akhtaruzzaman, N. Amin, K. Sopian, Emerging sustainable solutions for depollution: Geopolymers, Constr. Build. Mater. 199 (2019) 540-548.

[6] W.M. Kriven, J.L. Bell, M. Gordon, Microstructure and microchemistry of fully-reacted geopolymers and geopolymer matrix composites, Ceram. Trans. 153 (2013) 227–250.

[7] E. Landi, V. Medri, E. Papa, J. Dedecek, P. Klein, P. Benito, A. Vaccari, Alkali-bonded ceramics with hierarchical tailored porosity, Appl. Clay Sci. 73 (2013) 56–64.

[8] O. Bortnovsky, J. Dedecek, Z. Tvaruzkova, Z. Sobalík, J. Subrt, Metal ions as probes for characterization of geopolymer materials, J. Am. Ceram. Soc. 91 (2008) 3052-3057.

[9] A.A. Siyal, M.R. Shamsuddin, M.I. Khan, N.E. Rabat, M. Zulfiqar, Z. Man, J. Siame, K.A. Azizli, A review on geopolymers as emerging materials for the adsorption of heavy metals and dyes, J. Environ. Manage. 224 (2018) 327-339.

[10] T. Luukkonen, A. Heponiemi, H. Runtti, J. Pesonen, J. Yliniemi, U. Lassi, Application of alkali-activated materials for water and wastewater treatment: a review, Rev. Environ. Sci. Biotechnol 18 (2019) 271-297.

[11] S.A. Rasaki, Z. Bingxue, R. Guarecucu, T. Thomas, Y. Minghui, Geopolymer for use in heavy metals adsorption, and advanced oxidative processes: A critical review, J. Clean. Prod. 213 (2019) 42-58.

[12] C. Bai, P. Colombo, Processing, properties and applications of highly porous geopolymers: A review, Ceram. Int. 44 (2018) 16103-16118.

[13] V. Medri, E. Papa, J. Dedecek, H. Jirglova, P. Benito, A. Vaccari, E. Landi, Effect of metallic Si addition on polymerization degree of in situ foamed alkali-aluminosilicates, Ceram. Int. 39 (2013) 7657–7668.

[14] R.M. Novais, J. Carvalheiras, D.M. Tobaldi, M.P. Seabra, R.C. Pullar, J.A. Labrincha, Synthesis of porous biomass fly ash-based geopolymer spheres for efficient removal of methylene blue from wastewaters, J. Clean. Prod. 207 (2019) 350-362.

[15] S. Deville, Freeze-casting of porous ceramics: A review of current achievements and issues, Adv. Eng. Mater. 10 (2008) 155–169.

[16] W.L. Li, K. Lu, J.Y. Walz, Freeze casting of porous materials: Review of critical factors in microstructure evolution, Int. Mater. Rev. 57 (2012) 37–60.

[17] Y. Ge, X. Cui, C. Liao, Z. Li, Facile fabrication of green geopolymer/alginate hybrid spheres for efficient removal of Cu(II) in water: Batch and column studies, Chem. Eng. J. 311 (2017) 126-134.

[18] Q. Tang, Y-Y. Ge, K-T. Wang, Y. He, X-M. Cui, Preparation of porous metakaolin-based inorganic polymer spheres as an adsorbent, Mater. Design 88 (2015) 1244-1249.

[19] Y. Ge, X. Cui, Y. Kong, Z. Li, Y. He, Q. Zhou, Porous geopolymeric spheres for removal of Cu(II) from aqueous solution: Synthesis and evaluation, J. Hazard. Mater. 283 (2015) 244-251.

[20] V. Medri, E. Papa, J. Lizion, E. Landi, 2019. Metakaolin-based geopolymer beads: Production methods and characterization, J. Clean. Prod. 244 (2020) 118844.

[21] E. Papa, V. Medri, A. Natali Murri, F. Miccio, E. Landi, Ice-templated geopolymer—Fe/Mn oxide composites conceived as oxygen carriers, Ceramics 2 (2019) 148–160.

[22] V. Medri, S. Fabbri, J. Dedecek, Z. Sobalik, Z. Tvaruzkova, A. Vaccari, Role of the morphology and the dehydroxylation of metakaolins on geopolymerization, Appl. Clay Sci. 50 (2010) 538-545.

[23] M. Minelli, V. Medri, E. Papa, F. Miccio, E. Landi, F. Doghieri, Geopolymers as solid adsorbent for CO_2 capture, Chem. Eng. Sci. 148 (2016) 267–274.

[24] E. Papa, V. Medri, P. Benito, A. Vaccari, S. Bugani, J. Jaroszewicz, W. Swieszkowski, E. Landi, Synthesis of porous hierarchical geopolymer monoliths by ice-templating, Microporous Mesoporous Mater. 215 (2015) 206–214.

[25] E. Papa, V. Medri, P. Benito, A. Vaccari, S. Bugani, J. Jaroszewicz, E. Landi, Insights into the macroporosity of freeze-cast hierarchical geopolymers, RSC Adv. 6 (2016) 24635–24644.

[26] M. Adda-Bedia, S. Kumar, F. Lechenault, S. Moulinet, M. Schillaci, D. Vella, Inverse Leidenfrost effect: levitating drops on liquid nitrogen, Langmuir 32 (2016) 4179-4188.

[27] L.A. Liljedahl, Effect of fluid properties and nozzle parameters on drop size distribution from fan spray nozzles, Retrospective Theses and Dissertations 4476 (1971) https://lib.dr.iastate.edu/rtd/4476

[28] Y. Zhang, K. Zhou, Y. Bao, D. Zhang, Effects of rheological properties on ice-templated porous hydroxyapatite ceramics, Mater. Sci. Eng. C 33 (2013) 340–346.

[29] J. Wang, Q. Gong, D. Zhuang, J. Liang, Chemical vapor infiltration tailored hierarchical porous CNTs/C composite spheres fabricated by freeze casting and their adsorption properties, RSC Adv. 5 (2015) 16870-16877.

[30] Y.S. Song, D. Adler, F. Xu, E. Kayaalp, A. Nureddin, R.M. Anchan, R.L. Maas, U. Demirci, Vitrification and levitation of a liquid droplet on liquid nitrogen, PNAS 107 (10) (March 9, 2010) 4596-4600.

[31] C.M. Pekor, P. Kisa, I. Nettleship, Effect of polyethylene glycol on the microstructure of freeze-cast alumina, J. Am. Ceram. Soc. 91 (2008) 3185-3190.

[32] C. Pekor, I. Nettleship, The effect of the molecular weight of polyethylene glycol on the microstructure of freeze-cast alumina, Ceram. Int. 40 (2014) 9171-9177.

[33] Y. Zhang, L. Liu, Fly ash-based geopolymer as a novel photocatalyst for degradation of dye from wastewater, Particuology 11 (2013) 353-358.

[34] M.I. Khan, T.K. Min, K. Azizli, S. Sufian, Z. Man, H. Ullah, Effective removal of methylene blue from water using phosphoric acid based geopolymer, RSC Adv. 5 (2015) 61410-61420.

[35] V. Vadivelan, K. Vasanth Kumar, Equilibrium, kinetics, mechanism, and process design for the sorption of methylene blue onto rice husk, J. Colloid Interf. Sci. 286 (2005) 90–100.

[36] D.B. Jiang, C. Jing, Y. Yuan, L. Feng, X. Liu, F. Dong, B. Dong, Y.X. Zhang, 2D-2D growth of NiFe LDH nanoflakes on montmorillonite for cationic and anionic dye adsorption performance, J. Colloid Interf. Sci. 540 (2019) 398-409.

Elettra Papa: Conceptualization, Investigation, Formal analysis, Writing - Original Draft. **Matteo Mor:** Methodology, Investigation, Formal analysis. **Annalisa Natali Murri:** Writing - Review & Editing. **Elena Landi:** Conceptualization, Writing - Review & Editing. **Valentina Medri:** Conceptualization, Supervision, Writing - Review & Editing.